

G-image Segmentation: Similarity-preserving Fuzzy C-Means with Spatial Information Constraint in Wavelet Space

Cong Wang, Witold Pedrycz, *Fellow, IEEE*, ZhiWu Li, *Fellow, IEEE*, MengChu Zhou, *Fellow, IEEE*, and Shuzhi Sam Ge, *Fellow, IEEE*

Abstract—G-images refer to image data defined on irregular graph domains. This work elaborates on a similarity-preserving Fuzzy C-Means (FCM) algorithm for G-image segmentation and aims to develop techniques and tools for segmenting G-images. To preserve the membership similarity between an arbitrary image pixel and its neighbors, a Kullback-Leibler divergence term on partition matrix is introduced as a part of FCM. As a result, similarity-preserving FCM is developed by considering spatial information of image pixels for its robustness enhancement. Due to superior characteristics of a wavelet space, the proposed FCM is performed in this space rather than Euclidean one used in conventional FCM to secure its high robustness. Experiments on synthetic and real-world G-images demonstrate that it indeed achieves higher robustness and performance than the state-of-the-art segmentation algorithms. Moreover, it requires less computation than most of them.

Index Terms—Fuzzy C-Means; G-image segmentation; spatial information; similarity-preserving; wavelet space.

I. INTRODUCTION

CLASSIC image segmentation involves an analysis or manipulation of image data defined in regular Euclidean domains [1]. In recent years, with rapid advances in information and computer technology, image data defined in irregular domains including complex topologies have received much attention [2]–[4]. Graphs positioned in high dimensional

This work was supported in part by the Doctoral Students' Short Term Study Abroad Scholarship Fund of Xidian University, in part by the National Natural Science Foundation of China under Grant Nos. 61873342, 61672400, 62076189, in part by the Recruitment Program of Global Experts, and in part by the Science and Technology Development Fund, MSAR, under Grant No. 0012/2019/A1. (*Corresponding author: ZhiWu Li and MengChu Zhou*.)

C. Wang is with the School of Electro-Mechanical Engineering, Xidian University, Xi'an 710071, China (e-mail: wangc0705@stu.xidian.edu.cn).

W. Pedrycz is with the Department of Electrical and Computer Engineering, University of Alberta, Edmonton, AB T6R 2V4, Canada, the School of Electro-Mechanical Engineering, Xidian University, Xi'an 710071, China, and also with the Faculty of Engineering, King Abdulaziz University, Jeddah 21589, Saudi Arabia (e-mail: wpedrycz@ualberta.ca).

Z. W. Li is with the School of Electro-Mechanical Engineering, Xidian University, Xi'an 710071, China, and also with the Institute of Systems Engineering, Macau University of Science and Technology, Macau, China (e-mail: zhwli@xidian.edu.cn).

M. C. Zhou is with the Institute of Systems Engineering, Macau University of Science and Technology, Macau 999078, China and also with the Helen and John C. Hartmann Department of Electrical and Computer Engineering, New Jersey Institute of Technology, Newark, NJ 07102 USA (e-mail: zhou@njit.edu).

S. S. Ge is with the Department of Electrical and Computer Engineering, National University of Singapore, Singapore 117576, and also with the Institute of Future, Qingdao University, Qingdao 266071, China (e-mail: samge@nus.edu.sg).

spaces offer a capacity to model such data and complex interactions among them [5]. They can be represented by randomly discretizing or sampling from smooth Riemannian manifolds [6], [7]. They are composed of vertices and (possibly weighted) edges connecting vertices. Generally speaking, a graph can model a network represented by its internal vertices.

Let us assume for now that an image defined on a graph can be modelled as a real-valued function residing on vertices. It can be simply referred to a G-image. It can be represented through various interacting objects, such as colors, labels, and coordinates. In addition, as a classic two-dimensional image, it stems from various domains. However, unlike a two-dimensional image, the underlying graph tells a fair amount about it through a graph structure. In conclusion, G-images extend the universe of discourse of classical image processing. In other words, the scope of investigation on image processing is extended from Euclidean domains to graph ones. Due to the nonlinear nature of graphs, it is challenging to design efficient computing methods for manipulating and processing G-images.

Although a G-image is a new term proposed for the first time, prior to this work, researchers have made some encouraging attempts to solve image processing problems defined on graphs [8]–[11]. For instance, Hammond et al. [8] construct wavelets on graphs via spectral graph theory and apply them to a variety of scenarios. Dong [9] reports a fast discrete tight wavelet frame transform defined on graphs and investigates some practical problems via it, such as graph denoising and graph clustering. Wang and Yang [10] come up with a weighted variational model for Poisson noise removal from images defined on graphs. More recently, Wang et al. [11] present a universal method for removing mixed or unknown noise from images on graphs. It is modeled by a weighted fidelity term and a regularization term of using a discrete wavelet frame transform on graphs to detect image feature details.

Inspired by the work mentioned above, in this paper, we focus on developing techniques and tools for segmenting G-images. The field that gathers this issue under a common umbrella is G-image segmentation. Specifically, it aims to segment images defined on irregular domains or high-dimensional spaces. To do so, it is an important task to extend classical image segmentation concepts and methods such as clustering [12], [13], watershed transform [14], Graph Cut [15], neural networks [16], and active contour modelling [17], to G-image

segmentation.

In this paper, we discuss how to improve fuzzy clustering methods and then apply them to G-image segmentation. As a commonly studied fuzzy clustering method, Fuzzy C-Means (FCM) plays a significant role in classical image segmentation [13]. Yet it is not robust to noise. To improve robustness, two main means are often used, i.e., considering spatial information in it [18]–[23] and substituting its Euclidean distance with a kernel distance (function) [24]–[28]. As a result, a large number of its modified versions have been put forward [18]–[28]. Although they make evident efforts on FCM’s robustness enhancement, they often suffer from high computing overhead of clustering. To maintain a good balance between performance and efficiency, some researchers have recently attempted to develop FCM by virtue of various techniques such as Kullback-Leibler (KL) divergence [29]–[31], sparse regularization [32]–[34], gray level histograms [35], morphological reconstruction [36], and image superpixel [37], thus resulting in some comprehensive FCM algorithms [30]–[37]. Even though many studies have been reported, there exist no deep discussion of optimizing a membership partition by preserving the membership similarity between an arbitrary image pixel and its neighbors.

In addition, in our earlier work [38], for the first time, we attempt to apply FCM to segment images defined on graph domains. However, the term “G-image” has never been coined. In [38], we propose Wavelet-frame-based FCM (WFCM) with spatial information constraint. We expanded FCM’s application fields instead of developing its mathematical theory. In addition, we failed to exploit the full use of spatial information to advance FCM. Therefore, despite its sound significance, WFCM’s segmentation performance remains to be improved.

Motivated by [38], we propose an improved FCM variant for G-image segmentation, which realizes the optimization of a partition matrix and fast clustering. Its framework is illustrated in Fig. 1.

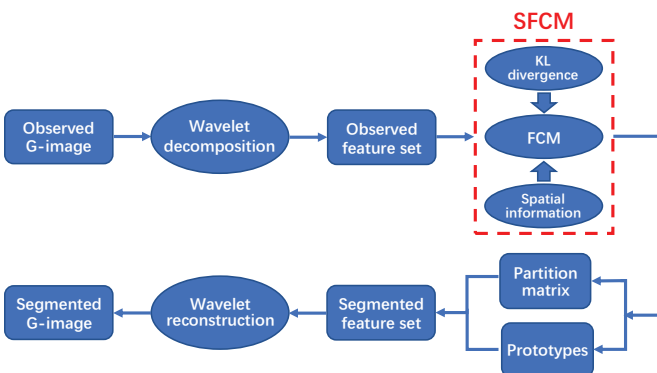


Fig. 1. The proposed framework for G-image segmentation.

Since a tight wavelet frame transform provides redundant representations of images [9], [10], [39]–[41], image features can be revealed in a wavelet space. As Fig. 1 shows, we employ tight wavelet frame decomposition to form the feature set associated with an observed G-image. Taking such set as data to be clustered, we augment FCM by introducing spatial information and a KL divergence term on a partition matrix,

thus resulting in Similarity-preserving FCM with spatial information constraint (SFCM). Spatial information is innovatively used to improve FCM’s robustness to noise and optimize data distribution. KL divergence is used to preserve the membership similarity between an arbitrary pixel and its neighbors. Based on a partition matrix and prototypes obtained by SFCM, a segmented G-image is reconstructed via tight wavelet frame reconstruction.

This work makes threefold contributions:

- It presents SFCM by virtue of spatial information and KL divergence. It is fast and robust FCM that realizes similarity preservation and noise suppression.
- It performs SFCM in a wavelet space produced by using a tight wavelet frame transform. Such space provides the superior analysis and manipulation of image details over non-robust Euclidean one that is used in conventional FCM and causes an undesired robustness issue.
- We apply SFCM to graph domains over Euclidean ones. Due to the nonlinear nature of graphs, SFCM offers a new avenue for G-image segmentation.

The originality of this work is to propose a fast and robust FCM algorithm for G-image segmentation, which preserves membership similarity between pixels and their neighbors in a wavelet space. To be specific, we make full use of spatial information in a graph structure, which can not only improve FCM’s robustness, but also make clustered data more reliable and applicable. In essence, the proposed FCM is a kernel-based FCM algorithm by treating wavelet frame transforms as a kernel function. In the kernel space, G-image features can be well found and analyzed. We preserve partition matrix similarity via KL divergence. Note that using KL divergence may bring more computing overheads. However, due to the positive effect of spatial information on optimizing data distributions, this shortcoming can be well offset.

This paper is arranged as follows. Section II briefly describes some preliminaries relevant to this work. Section III formulates the proposed methodology. Section IV illustrates experimental results. Conclusions and some open issues are covered in Section V.

II. PRELIMINARIES

In this section, we briefly introduce three basic concepts involved in this work, i.e., spectral graph theory, tight wavelet frame transform, and FCM. Interested readers can find more details in [9], [38], [42].

A. Spectral Graph Theory

A weighted graph $G = (V, E, \omega)$ defined in a domain $\Omega = \{1, 2, \dots, K\}$ is composed of a vertex set $V = \{v_i : i \in \Omega\}$ collecting (x, y, z) -coordinates of K vertices, an edge set $E = \{(v_i, v_j) : i, j \in \Omega \text{ and } i \neq j\}$, and a weight function $\omega : E \mapsto \mathbb{R}^+$ that assigns a positive weight ω_{ij} to each edge (v_i, v_j) [9]:

$$\omega_{ij} = \exp(-\|v_i - v_j\|^2/\rho), \quad (1)$$

where ρ is a positive parameter and $\|\cdot\|$ denotes the Euclidean distance between v_i and v_j . Since G is undirected, we have $\omega_{ij} = \omega_{ji}$.

G 's adjacency matrix is denoted as $\mathbf{A} = [a_{ij}]_{K \times K}$ with

$$a_{ij} = \begin{cases} \omega_{ij}, & \text{if } v_i \text{ and } v_j \text{ are connected} \\ 0, & \text{otherwise} \end{cases}.$$

G 's degree matrix is expressed as $\mathbf{D} = \text{diag}\{d_i = \sum_j a_{ij} : i, j \in \Omega\}$, where d_i represents the degree of vertex v_i . Its Laplacian matrix can be defined as

$$\mathbf{L} = \mathbf{D} - \mathbf{A}.$$

K pairs of eigenvalues and eigenvectors of \mathbf{L} are denoted as $\{(\lambda_i, e_i) : i \in \Omega\}$. Since \mathbf{L} is symmetric and positive semidefinite, we have $\lambda_K \geq \dots \geq \lambda_i \geq \dots \geq \lambda_2 > \lambda_1 = 0$.

We define a real-valued function on G as $\mathbf{g} : V \mapsto \mathbb{R}$. It can be modeled as a collection of discrete data, i.e., $\{g(v_i) \in [0, 1] : i \in \Omega\}$. To make it easily understood, we take an example ‘bunny’ to intuitively portray it, as shown in Fig. 2.

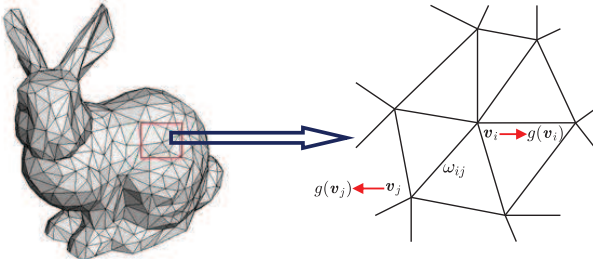


Fig. 2. Illustration of G and \mathbf{g} .

B. Tight Wavelet Frame Transform on Graph

Given is a graph $G = (V, E, \omega)$ and a function $\mathbf{g} : V \mapsto \mathbb{R}$ defined on it. Next, we briefly introduce a tight wavelet frame transform of \mathbf{g} . In a concise way, for $i \in \Omega$, $g(v_i) \in \mathbf{g}$ is rewritten as $g[i]$. The Fourier transform of \mathbf{g} is denoted as $\hat{\mathbf{g}}$ with the element:

$$\hat{g}[i] = \sum_{j=1}^K g[j]e_{ij},$$

where e_{ij} is the j -th element of e_i .

Given a finite set of masks $\{h_b : 0 \leq b \leq \mathcal{B}\}$, their Fourier series are denoted as $\{\hat{h}_b\}$. \hat{h}_b^* stands for the complex conjugate of \hat{h}_b . The \mathfrak{L} -level wavelet frame decomposition is defined as

$$\mathcal{W}\mathbf{g} := \{\mathcal{W}_{b,l}\mathbf{g} : (b, l) \in \mathbb{B}\}$$

with

$$\mathbb{B} := \{(1, 1), (2, 1), \dots, (\mathcal{B}, 1), (1, 2), \dots, (\mathcal{B}, \mathfrak{L})\} \cup \{(0, \mathfrak{L})\},$$

where \mathcal{W} is a decomposition operator. In a Fourier domain, it can be expressed as

$$\widehat{\mathcal{W}_{b,l}\mathbf{g}}[i] = \begin{cases} \hat{h}_b^*(2^{-s}\lambda_i) \hat{g}[i] & l = 1 \\ \hat{h}_b^*(2^{-s+l-1}\lambda_i) \hat{h}_0^*(2^{-s+l-2}\lambda_i) \\ \dots \hat{h}_0^*(2^{-s}\lambda_i) \hat{g}[i] & 2 \leq l \leq \mathfrak{L} \end{cases}, \quad (2)$$

where s is the dilation scale being the smallest integer such that $\lambda_K \leq 2^s\pi$.

Let $\mathcal{R} := \mathcal{W}\mathbf{g} := \{\mathcal{R}_{b,l}, (b, l) \in \mathbb{B}\}$ with $\mathcal{R}_{b,l} := \mathcal{W}_{b,l}\mathbf{g}$ be the tight wavelet frame coefficients of \mathbf{g} . For $l = \mathfrak{L}, \mathfrak{L} -$

$1, \dots, 1\}$, the wavelet frame reconstruction $\mathcal{W}^T\mathcal{R}$ is defined by the following iterative procedure in a frequency domain:

$$\widehat{\mathcal{R}}_{0,l-1}[i] := \sum_b \hat{h}_b(2^{-s+l-1}\lambda_i) \widehat{\mathcal{R}}_{b,l}[i], \quad (3)$$

where $\mathcal{R}_{0,0} = \mathcal{W}^T\mathcal{R}$ is the reconstructed data from \mathcal{R} and \mathcal{W}^T is a reconstruction operator. As Theorem 3.1 in [9] indicates, $\mathcal{W}^T\mathcal{W} = \mathcal{I}$ is obtained, where \mathcal{I} is an identity matrix, thus implying that a tight wavelet frame transform can realize the accurate reconstruction of data.

As (2) and (3) show, all eigenvalues $\{\lambda_i : i \in \Omega\}$ of the graph Laplacian matrix \mathbf{L} are needed. However, they are hard to be computed since the size of \mathbf{L} is large. To address this issue, the masks $\{h_b\}$ are accurately approximated by low-degree Chebyshev polynomials [43] since their Fourier series $\{h_b\}$ are trigonometric polynomials [9]. In this case, it is not needed to compute all eigenvalues $\{\lambda_i : i \in \Omega\}$. Therefore, the use of Chebyshev polynomials makes the tight wavelet frame transform easily executable. The details can be found in [9] and [38].

C. Fuzzy C-Means (FCM)

For a domain $\Omega = \{1, 2, \dots, K\}$, FCM is used to divide a data pattern $\mathbf{X} = \{\mathbf{x}_i : i \in \Omega\}$ into c clusters by minimizing the objective function:

$$J(\mathbf{U}, \mathbf{Y}) = \sum_{i=1}^K \sum_{j=1}^c u_{ij}^m \|\mathbf{x}_i - \mathbf{y}_j\|^2, \quad (4)$$

where $\mathbf{U} = [u_{ij}]_{K \times c}$ is a partition matrix with a constraint $\sum_{j=1}^c u_{ij} = 1$ for $\forall i$ and $0 < \sum_{i=1}^K u_{ij} < K$ for $\forall j$, $\mathbf{Y} = \{\mathbf{y}_j\}_{j=1,2,\dots,c}$ is a prototype set, m is a fuzzification exponent ($m > 1$), and $\|\cdot\|$ denotes the Euclidean distance.

An alternating iteration scheme [42] is employed to minimize (4), which is realized as follows:

$$u_{ij}^{(t+1)} = \frac{(\|\mathbf{x}_i - \mathbf{y}_j^{(t)}\|^2)^{-1/(m-1)}}{\sum_{q=1}^c (\|\mathbf{x}_i - \mathbf{y}_q^{(t)}\|^2)^{-1/(m-1)}},$$

$$\mathbf{y}_j^{(t+1)} = \frac{\sum_{i=1}^K (u_{ij}^{(t+1)})^m \mathbf{x}_i}{\sum_{i=1}^K (u_{ij}^{(t+1)})^m}.$$

Here, t is an iterative step. If $\|\mathbf{U}^{(t+1)} - \mathbf{U}^{(t)}\|$ is less than a threshold ε , the FCM algorithm terminates.

III. PROPOSED METHODOLOGY

In this section, we formulate the proposed methodology for G-image segmentation. It consists of three key parts, i.e., spatial information, wavelet space, and similarity-preserving FCM.

A. Spatial Information Description

Consider a graph $\mathbf{G} = (\mathbf{V}, \mathbf{E}, \omega)$ defined in a domain $\Omega = \{1, 2, \dots, K\}$ and an observed G-image \mathbf{g} defined on \mathbf{G} . In this work, we discuss how to segment \mathbf{g} so as to obtain a segmented G-image $\tilde{\mathbf{g}}$. To make them easier to be understood, we still take ‘bunny’ in Fig. 2 to intuitively show them, as seen from Fig. 3.

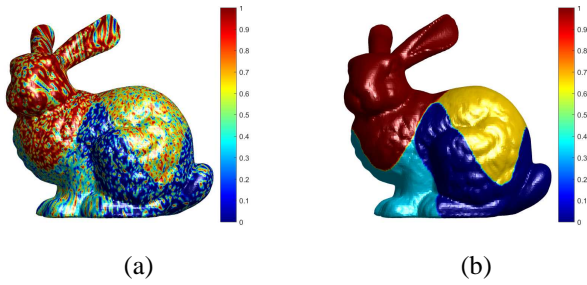


Fig. 3. Illustration of G-images on graph \mathbf{G} . (a) observed G-image and (b) segmented G-image.

For an arbitrary pixel $g[i] \in \mathbf{g}$ with $i \in \Omega$, its value is nearer to ones of its neighbors. To better debase the effect of noise, it is important to take spatial information into account for G-image segmentation. We here illustrate spatial information of $g[i]$, as shown in Fig. 4.

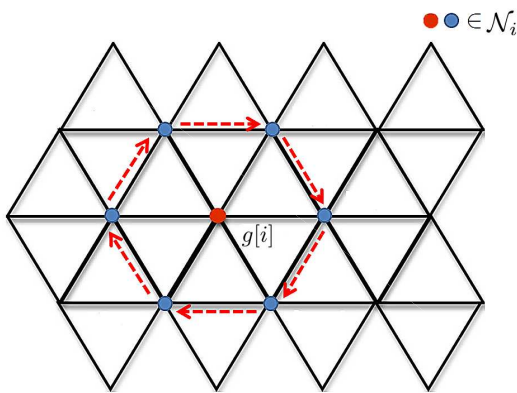


Fig. 4. Illustration of spatial information of $g[i]$.

Fig. 4 exhibits a flat representation of the local topological structure of a graph. Red dot represents a center $g[i]$ being the i th G-image pixel. Its gray value is defined in a unit interval $[0, 1]$. To correspond to classic two-dimensional images, the gray value is usually rescaled to an intensity ranging from 0 to 255 in the experiment. The neighbor pixels of $g[i]$ are described by blue dot. \mathcal{N}_i indicates the spatial information centralized in $g[i]$, which contains center $g[i]$ and its neighbor pixels. Since $g[i]$ is nearer to its neighbors, they generally have similar membership grades. Therefore, the use of spatial information is beneficial to the performance improvement of G-image segmentation.

B. Wavelet Space Formation

As (2) indicates, when forming a wavelet space of G-images, a critical step is to choose a tight frame system or a sequence of masks. The findings of [39] and [44] show that

a piecewise linear B-spline tight frame system is adaptable to image features or noise interference. Furthermore, it has a simple explicit expression for redundant representations of images, which makes image details better found and retained. In this work, we employ it including three masks h_0 , h_1 , and h_2 . For $\xi \in [0, \pi]$, the Fourier transforms of such masks are expressed as

$$\hat{h}_0(\xi) = \cos^2\left(\frac{\xi}{2}\right), \hat{h}_1(\xi) = \frac{1}{\sqrt{2}} \sin(\xi), \hat{h}_2(\xi) = \sin^2\left(\frac{\xi}{2}\right). \quad (5)$$

By combining (2) and (5), a decomposition operator \mathbf{W} can be realized. To be specific, (5) exhibits one low-pass mask h_0 and two high-pass masks h_1 and h_2 . Once the transform level \mathcal{L} is given, tight wavelet frame coefficients of \mathbf{g} are formulated as

$$\mathbf{W}\mathbf{g} = \{\mathcal{W}_{0,\mathcal{L}}\mathbf{g}, \mathcal{W}_{1,1}\mathbf{g}, \mathcal{W}_{2,1}\mathbf{g}, \mathcal{W}_{1,2}\mathbf{g}, \dots, \mathcal{W}_{2,\mathcal{L}}\mathbf{g}\}. \quad (6)$$

Such coefficients in (6) constitute the feature set \mathbf{X} associated with \mathbf{g} , i.e., $\mathbf{X} = \mathbf{W}\mathbf{g}$. For image segmentation, the wavelet frame coefficient $\mathcal{W}_{0,\mathcal{L}}\mathbf{g}$ is low-frequency information, the rest represent high-frequency information. Hence, (6) describes a wavelet space formed by using \mathcal{L} -level tight wavelet frame decomposition. To visually exhibit the wavelet space, we use an example shown in Fig. 5.

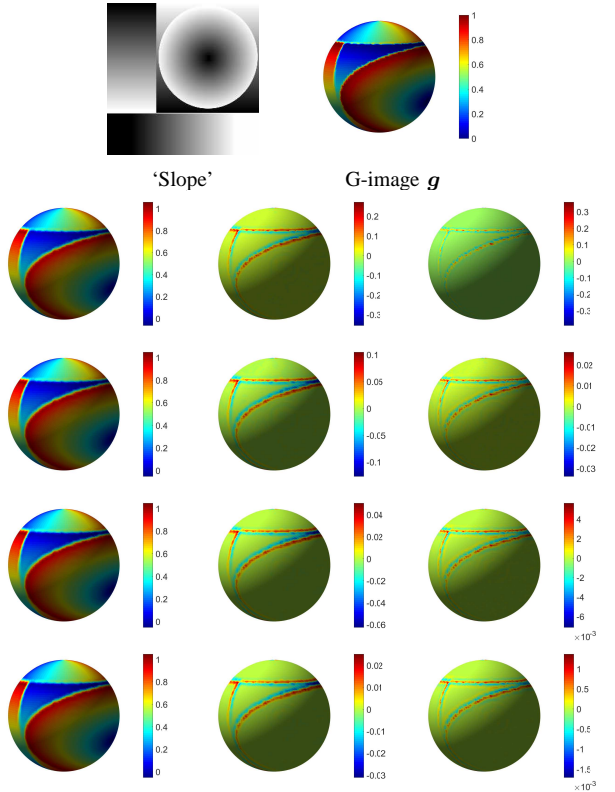


Fig. 5. Illustration of tight wavelet frame coefficients $\{\mathcal{W}_{b,l}\mathbf{g}\}$ for $0 \leq b \leq 2$ (column 1–3) and $1 \leq l \leq 4$ (row 1–4).

As Fig. 5 shows, in the first row, an image ‘Slope’ is mapped to a unit sphere to form a G-image \mathbf{g} . The rest rows present tight wavelet frame coefficients with different transform levels. Since there exist some geometrical structures in a G-image, its features (edges and textures) are not randomly distributed. The

second and third columns of Fig. 5 except the first row show G-image features detected by the tight frame system (5). Such features are spatially described and correlated. By performing the tight frame system (5), G-image features can be easily found and manipulated.

C. Similarity-preserving FCM with Spatial Information Constraint (SFCM)

According to (6), we rewrite the feature set associated with \mathbf{g} as $\mathbf{X} = \mathcal{W}\mathbf{g} = \{\mathcal{W}_{0,i}\mathbf{g}, \mathcal{W}_{1,i}\mathbf{g}, \mathcal{W}_{2,i}\mathbf{g}\} = \{\mathbf{x}_i : i \in \Omega\}$. Based on (5), we have $\mathbf{x}_i = \{x_{i1}, x_{i2}, x_{i3}\} \in \mathbb{R}^3$. Hence, the size of \mathbf{X} is $K \times 3$. To preserve the membership similarity among pixels, we introduce a KL divergence term on membership partition as a part of FCM. By combining spatial information and KL divergence, we propose Similarity-preserving FCM with spatial information constraint (SFCM). Its objective function is expressed as

$$\begin{aligned} J(\mathbf{U}, \mathbf{Y}, \bar{\mathbf{U}}) = & \sum_{i=1}^K \sum_{j=1}^c u_{ij} \left(\sum_{n \in \mathcal{N}_i} \omega_{ni} \|\mathbf{x}_n - \mathbf{y}_j\|^2 \right) \\ & + \alpha \sum_{i=1}^K \sum_{j=1}^c u_{ij} \log \frac{u_{ij}}{\bar{u}_{ij}}, \end{aligned} \quad (7)$$

such that

$$\forall i \in \Omega : \sum_{j=1}^c u_{ij} = 1.$$

For the sake of convenience, a pixel or vertex is loosely represented by its corresponding index. Thus, $n \in \mathcal{N}_i$ in (7) denotes the neighbor pixels or vertices including i . ω_{ni} in (7) is a weight assigned to the edge between n and i , which is computed via (1). Moreover, α in (7) is a positive parameter to control the effect of KL divergence term $\sum_{i=1}^K \sum_{j=1}^c u_{ij} \log \frac{u_{ij}}{\bar{u}_{ij}}$ on the results of FCM. Here, we introduce a new variable $\bar{\mathbf{U}} = [\bar{u}_{ij}]_{K \times c}$ that is referred to a filtered partition matrix, where \bar{u}_{ij} is a weighted average on u_{ij} , and can be computed over spatial information \mathcal{N}_i around u_{ij} . It is given as

$$\bar{u}_{ij} = \frac{\sum_{n \in \mathcal{N}_i} \omega_{ni} u_{nj}}{\sum_{n \in \mathcal{N}_i} \omega_{ni}}. \quad (8)$$

Eq. (8) indicates that abnormal membership grade u_{ij} is corrected by the related neighbors. The KL divergence term aims to keep a sound similarity between u_{ij} and \bar{u}_{ij} . Hence, with many iterations, the optimal partition matrix \mathbf{U} is computed. In addition, from (7), we see that the value of the fuzzification exponent m has been fixed at $m = 2$.

In particular, we note that in [29], KL divergence is first applied to FCM in classic image segmentation. However, our work is very different from [29]. To be specific, we focus on G-image segmentation rather than classic image segmentation. In [29], the mean filtering is used to produce \bar{u}_{ij} and its result is worse than that of our weighted average filtering (8). We present a novel objective function (7) by virtue of spatial information and KL divergence, which is different from and

superior to the one reported in [29]. In addition, [29] exhibits a high computing overhead due to its failure to use spatial information. Our work offsets this shortcoming of [29].

From (7), we see that its minimization involves three components, i.e., \mathbf{U} , \mathbf{Y} and $\bar{\mathbf{U}}$. As (8) indicates, $\bar{\mathbf{U}}$ can be automatically determined by \mathbf{U} . Therefore, we design a two-step iterative algorithm for minimizing (7), where $\bar{\mathbf{U}}$ is first fixed to compute \mathbf{U} and \mathbf{Y} , then \mathbf{U} is used to update $\bar{\mathbf{U}}$. The main task in each iteration is to solve the minimization problem in terms of \mathbf{U} and \mathbf{Y} when fixing $\bar{\mathbf{U}}$. Assume that $\bar{\mathbf{U}}$ is given. We apply a Lagrangian multiplier method to minimize (7). The augmented function is formulated as

$$\begin{aligned} \mathcal{L}_{\Xi}(\mathbf{U}, \mathbf{Y}; \bar{\mathbf{U}}) = & \sum_{i=1}^K \sum_{j=1}^c u_{ij} \left(\sum_{n \in \mathcal{N}_i} \omega_{ni} \|\mathbf{x}_n - \mathbf{y}_j\|^2 \right) \\ & + \alpha \sum_{i=1}^K \sum_{j=1}^c u_{ij} \log \frac{u_{ij}}{\bar{u}_{ij}} + \sum_{i=1}^K \xi_i \left(\sum_{j=1}^c u_{ij} - 1 \right), \end{aligned}$$

where $\Xi = \{\xi_i : i \in \Omega\}$ collects K Lagrangian multipliers. We realize a two-step iterative algorithm for minimizing (7) as Algorithm 1.

Algorithm 1 Two-step iterative algorithm

Given a threshold ε , input $\bar{\mathbf{U}}^{(0)}$. For $t = 0, 1, \dots$, iterate:

Step 1: Find minimizers $\mathbf{U}^{(t+1)}$ and $\mathbf{Y}^{(t+1)}$:

$$(\mathbf{U}^{(t+1)}, \mathbf{Y}^{(t+1)}) = \arg \min_{\mathbf{U}, \mathbf{Y}} \mathcal{L}_{\Xi}(\mathbf{U}, \mathbf{Y}; \bar{\mathbf{U}}^{(t)}). \quad (9)$$

Step 2: Update the filtered partition matrix $\bar{\mathbf{U}}^{(t+1)}$.

If $\|\mathbf{U}^{(t+1)} - \mathbf{U}^{(t)}\| < \varepsilon$, stop; else update t such that $0 \leq t \uparrow < +\infty$.

Intuitively, the minimization problem (9) includes the following two subproblems:

$$\begin{cases} \mathbf{U}^{(t+1)} = \arg \min_{\mathbf{U}} \mathcal{L}_{\Xi}(\mathbf{U}, \mathbf{Y}^{(t)}; \bar{\mathbf{U}}^{(t)}) \\ \mathbf{Y}^{(t+1)} = \arg \min_{\mathbf{Y}} \mathcal{L}_{\Xi}(\mathbf{U}^{(t+1)}, \mathbf{Y}; \bar{\mathbf{U}}^{(t)}) \end{cases}. \quad (10)$$

There exists a closed-form solution to either subproblem in (10). We apply an alternative optimization scheme to optimize \mathbf{U} and \mathbf{Y} , which was first proposed in [42] to realize FCM. Therefore, the iterative updates of \mathbf{U} and \mathbf{Y} are realized as:

$$u_{ij}^{(t+1)} = \frac{\bar{u}_{ij}^{(t)} \exp \left(- \sum_{n \in \mathcal{N}_i} \omega_{ni} \|\mathbf{x}_n - \mathbf{y}_j^{(t)}\|^2 / \alpha \right)}{\sum_{q=1}^c \bar{u}_{iq}^{(t)} \exp \left(- \sum_{n \in \mathcal{N}_i} \omega_{ni} \|\mathbf{x}_n - \mathbf{y}_q^{(t)}\|^2 / \alpha \right)}, \quad (11)$$

$$\mathbf{y}_j^{(t+1)} = \frac{\sum_{i=1}^K \left(u_{ij}^{(t+1)} \sum_{n \in \mathcal{N}_i} \omega_{ni} \mathbf{x}_n \right)}{\sum_{i=1}^K \left(u_{ij}^{(t+1)} \sum_{n \in \mathcal{N}_i} \omega_{ni} \right)}. \quad (12)$$

To indicate the effect of KL divergence on the algorithm performance, we cover a case, as shown in Fig. 6. In this case, we impose 40% impulse noise to a noise-free G-image

(see Fig. 6(a)) including four levels (0, 1/3, 2/3 and 1), thus resulting in an observed (noisy) G-image shown in Fig. 6(b). To exhibit the positive effect of KL divergence, we compare SFCM with FCM while both spatial information and wavelet space are present. Their membership partitions are illustrated in Figs. 6(c) and (d), respectively. Obviously, SFCM makes more suitable membership partitions over FCM since KL divergence preserves the similarity between a pixel and its neighbors. It also reduces classification errors.

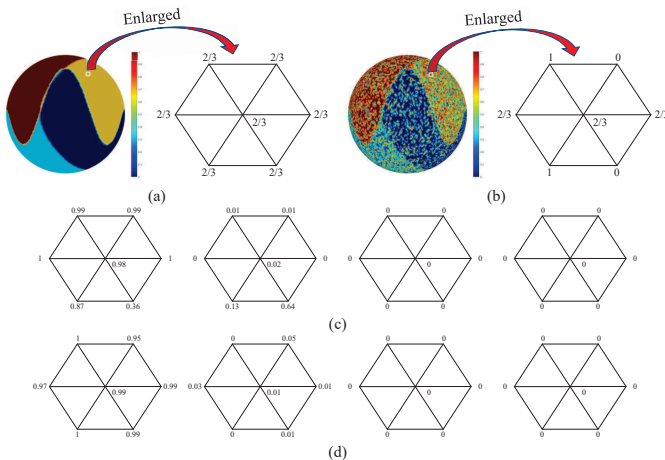


Fig. 6. Comparison of partition matrices generated by FCM and SFCM. (a) noise-free G-image; (b) observed G-image; (c) membership partitions of FCM; and (d) membership partitions of SFCM.

Once partition matrix \mathbf{U} and prototype \mathbf{Y} have been optimized, a segmented feature set $\widetilde{\mathbf{X}}$ is obtained. Based on it, a segmented G-image $\tilde{\mathbf{g}}$ is reconstructed:

$$\tilde{\mathbf{g}} = \mathbf{W}^T(\widetilde{\mathbf{X}}), \quad (13)$$

where \mathbf{W}^T is a wavelet frame reconstruction operator computed by (3). Therefore, the proposed algorithm for G-image segmentation is executed via Algorithm 2.

Algorithm 2 Similarity-preserving FCM with spatial information constraint in wavelet spaces (SFCM)

Input: Observed G-image \mathbf{g} , number of clusters c , and threshold ε .

Output: Segmented G-image $\tilde{\mathbf{g}}$.

- 1: Calculate the feature set \mathbf{X} via (6)
 - 2: Initialize randomly the filtered partition matrix $\overline{\mathbf{U}}^{(0)}$ and the prototypes $\mathbf{Y}^{(0)}$
 - 3: $t \leftarrow 0$
 - 4: **repeat**
 - 5: Calculate the partition matrix $\mathbf{U}^{(t+1)}$ via (11)
 - 6: Update the prototypes $\mathbf{Y}^{(t+1)}$ via (12)
 - 7: Update the filtered partition matrix $\overline{\mathbf{U}}^{(t+1)}$ via (8)
 - 8: $t \leftarrow t + 1$
 - 9: **until** $\|\mathbf{U}^{(t+1)} - \mathbf{U}^{(t)}\| < \varepsilon$
 - 10: **return** \mathbf{U} , \mathbf{Y} , and $\overline{\mathbf{U}}$
 - 11: Calculate the segmented feature set $\widetilde{\mathbf{X}}$ via \mathbf{U} and \mathbf{Y}
 - 12: Generate the segmented image $\tilde{\mathbf{g}}$ via (13)
-

D. Convergence Analysis

In this subsection, we analyze the convergence of SFCM. Just for the sake of intuition, we cover it by taking Fig. 5 as a case study. As Algorithm 2 shows, the termination condition of SFCM is $\|\mathbf{U}^{(t+1)} - \mathbf{U}^{(t)}\| < \varepsilon$. The threshold ε is set to 1×10^{-6} . In Fig. 7, we plot the curves of $\phi = \|\mathbf{U}^{(t+1)} - \mathbf{U}^{(t)}\|$ and J versus iteration t , respectively.

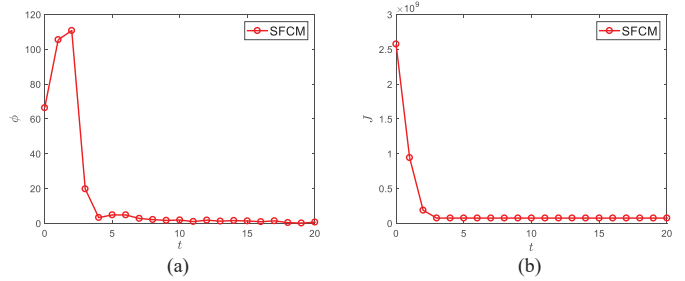


Fig. 7. Convergence of SFCM. (a) ϕ and (b) J versus t .

From Fig. 7(a), we can find that ϕ initially increases in a short time, and then quickly decreases to the value lower than ε . The increase of ϕ is due to the prototypes being randomly initialized. As Fig. 7(b) shows, however, J presents a descending process all the time, which means that the segmentation result of SFCM becomes better and better iteration proceeds.

IV. EXPERIMENTAL STUDIES

In this section, we provide supporting experiments for showing the effectiveness and robustness of SFCM. We first test it and six FCM-related algorithms via many synthetic and real-world G-images. Its peers include two variants of FCM with spatial information (namely FCM_S1 [19] and FCM_S2 [19]), fast generalized FCM (FGFCM) [21], weighted-fuzzy-factor and kernel-metric-based fuzzy local information c-means (termed as KWFLICM for short) [24], wavelet-frame-based FCM (WFCM) [38], and deviation-sparse FCM with neighbor information constraint (DSFCM_N) [33]. These algorithms have different advantages. FCM_S1, FCM_S2, and FGFCM are three classic FCM algorithms with spatial information constraint and have low computing overheads. KWFLICM and DSFCM_N have a strong capability of noise removal, while KWFLICM is a kernel-based FCM algorithm. WFCM is an FCM variant that we proposed earlier for segmenting images on graph domains. To further verify SFCM's strong robustness, we compare SFCM with two competing approaches unrelated to FCM, i.e., PFE [45] and AMR_SC [46], as illustrated at the end of this section. The results are evaluated by using three standard criteria: Segmentation accuracy (SA), Sorenson-Dice similarity (SDS), and Matthews correlation coefficient (MCC), as summarized in [47]–[49].

A. Parameter Selection

We first report how to set the parameters needed in these algorithms. Since AMR_SC and PFE are not related to FCM, we follow their parameter settings introduced in their original articles [45], [46]. In the following, we focus on all FCM-related algorithms. Due to the presence of spatial information,

we select a local window \mathcal{N}_i shown in Fig. 4 for all algorithms. We set the fuzzification exponent m and threshold ε to 2 and 1×10^{-6} , respectively. Except the above common parameters, we clarify their special parameters that are optimal in the experiment. In FCM_S1 and FCM_S2, α is set to 3.8, which aims to control the effect of spatial information. For FGFCM, the spatial scale factor λ_s and the gray-level scale factor λ_g are set to 3 and 5, respectively. KWFLICM has no other parameters. In WFCM, μ is used to maintain the interest of spatial information and thus is determined from 0.55 to 0.65. As to DSFCM_N, ℓ_1 vector norm is used and λ is set to $\delta/4$, where δ is the standard deviation of G-image data.

Next, we present the parameter selection of SFCM. As (7) indicates, the fuzzification exponent m in SFCM is fixed to 2. According to [9], ρ in (1) is equal to 10, where a tight wavelet frame transform with good redundant representation performance is obtained. We set the wavelet frame transform level \mathcal{L} in (6) to 1 since using a higher level only slightly furthers FCM's performance while the running time increases significantly. As said in Section II-B, using low-degree Chebyshev polynomials to approximate masks $\{\hat{h}_b\}$ in (5) can make the tight wavelet frame transform easily executed. By [9], the degree of Chebyshev polynomials is equal to 7.

α in (7) is an important user-defined parameter, which is used to control the effect of a KL divergence term on the results of FCM. Its setting process is described as follows: Due to each G-image pixel value belonging to $[0, 1]$, the order of magnitude of an arbitrary distance $\|\mathbf{x}_i - \mathbf{y}_j\|^2$ is 10^{-2} . In all experiments, to correspond to classic two-dimensional images, we usually rescale all G-images to an intensity ranging from 0 to 255. As a result, the order of magnitude of the distance $\|\mathbf{x}_i - \mathbf{y}_j\|^2$ generally goes up to 10^2 . To balance the effect of a KL divergence term in (7) on the results of FCM, α in (7) should be set to greater than 1×10^2 . Generally speaking, most of G-image pixels have six neighbors, i.e., $n = 7$ in (7). Since weight ω_{ni} is less than or equal to 1, α should be adjusted to be less than 7×10^2 . To sum up, in most cases, we have $\alpha \in (100, 700)$. In Fig. 8, as a case study, we report the setting process of α when segmenting a G-image (see Fig. 9(a)) contaminated by impulse noise.

As Figs. 8(a)–(c) indicates, with the increase of impulse noise levels (probability $\eta\%$), the values of SA, SDS, and MCC all become worse. For a certain noise level, as α increases, they always get better until they no longer change apparently. To sum up, large α yields excellent results. However, by taking $\eta = 40$ as a case, we find that more iterations are triggered when selecting larger α , as shown in Fig. 8(d). To keep a good tradeoff between performance and computation, we choose $\alpha = 350$ for a case $\eta = 40$.

B. Ablation Studies and Analysis

There are three main components involved in SFCM, i.e., spatial information, wavelet space, and KL divergence. We provide ablation studies to analyze their impacts on SFCM performance. We respectively segment five graphs images (see Fig. 9) with 40% impulse noise. The average segmentation results are presented in Table I. Symbol \checkmark represents that a component is present while symbol \times stands for its absence.

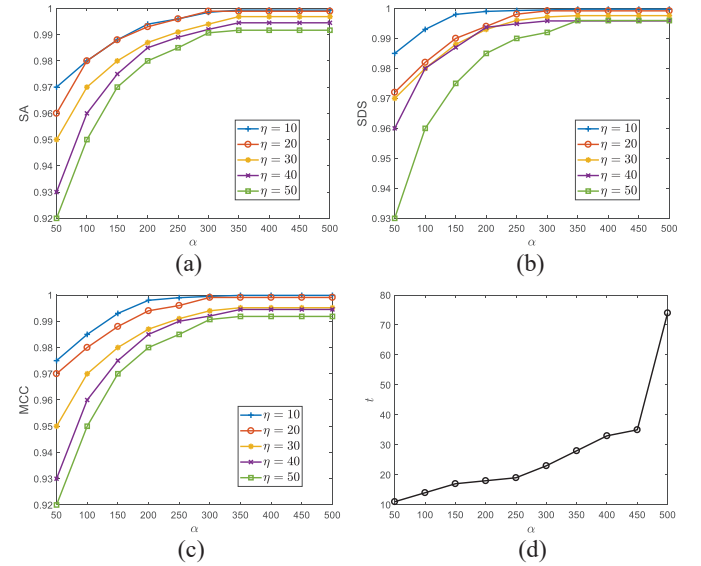


Fig. 8. Segmentation results with changes of α in presence of different levels of impulse noise.

TABLE I
INVESTIGATION OF EACH COMPONENT IN SFCM

Spatial information	Wavelet space	KL divergence	SA	Iterations
\times	\times	\times	0.917	15
\checkmark	\times	\times	0.929	19
\times	\checkmark	\times	0.940	14
\times	\times	\checkmark	0.977	30
\checkmark	\checkmark	\times	0.948	18
\checkmark	\times	\checkmark	0.982	25
\times	\checkmark	\checkmark	0.989	28
\checkmark	\checkmark	\checkmark	0.995	22

As Table I shows, we report the performance of SFCM with eight different combinations of three above components. Based on (7), when KL divergence is not considered, α should be equal to 0. However, from (11), SFCM is not executable when $\alpha = 0$. Hence, we set α to 50 for approximating the case that KL divergence is absent. In a wavelet space, the performance of SFCM is apparently improved. More importantly, KL divergence has the greatest impact on the performance enhancement of SFCM. However, it leads to more iterations. Since the use of spatial information makes data distributions optimized to be easily clustered, the iterations reduce. Therefore, the computing overhead of SFCM is not high.

C. Results on Synthetic G-images

We test two groups of synthetic G-images. For a fair comparison, all images are rescaled to an intensity ranging from 0 to 255. In the first experiment, we map five images onto a unit sphere, as shown in Fig. 9. For synthetic G-images, the number of clusters is known based on their gray level histograms. In general, the number of clusters is set to the number of peaks of the gray level histogram. In this experiment, the numbers of clusters c in (7) are 4, 4, 4, 3, and 3, respectively. We exhibit the average results for segmenting

such G-images in presence of different types of noises at different levels (Gaussian noise with standard deviation σ ; and impulse noise with probability $\eta\%$). They are summarized in Fig. 10. For a visual analysis, we show a case in Fig. 11.

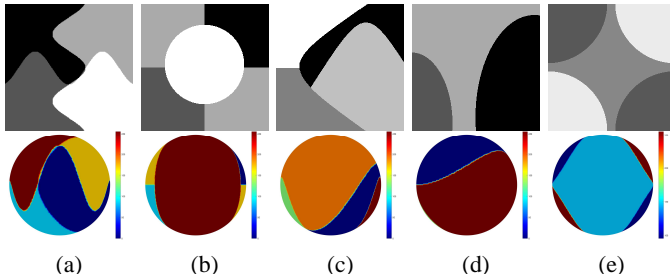


Fig. 9. Five synthetic G-images.

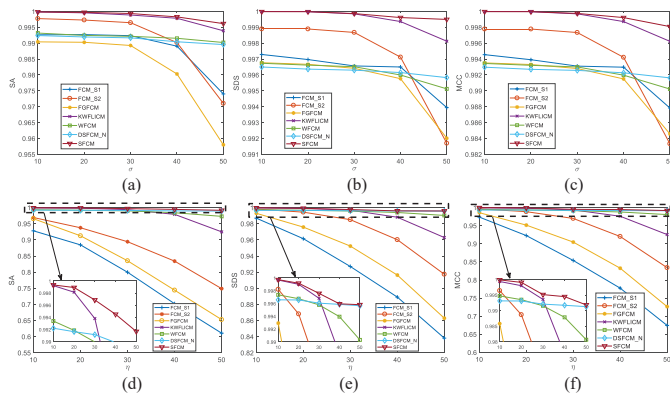


Fig. 10. Average segmentation results on five synthetic G-images corrupted by different types of noises at different levels.

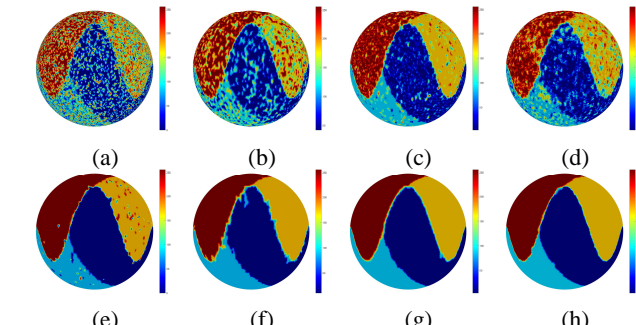


Fig. 11. Segmentation results on synthetic G-image (Fig. 9(a)) corrupted by impulse noise ($\eta = 40$ and $\alpha = 350$). From (a) to (h): observed G-image and results of FCM_S1, FCM_S2, FGFCM, KWFLICM, WFCM, DSFCM_N, and SFCM.

As Fig. 10 indicates, all algorithms can get over Gaussian noise of low levels effectively. KWFLICM outperforms other peers except SFCM. When the noise level is extremely high, only the results of SFCM remain at a good level. In presence of impulse noise, FCM_S1, FCM_S2 and FGFCM perform poorly. As the noise levels increase, the segmentation results of other algorithms also become worse. Among them, SFCM still works the best. From Fig. 11, we intuitively find that SFCM not only removes impulse noise of high levels well, but also retains more image features.

Due to a unit sphere having regular topological structure, segmenting images defined on it is not generally hard. In the second experiment, to exhibit the capacity of SFCM to cope with images on graphs including complex topologies, we select ten different graphs coming from Stanford 3D Scanning Repository¹. We map the two-dimensional image (Fig. 9(a)) onto them, thus producing ten G-images, as shown in Fig. 12. We set $c = 4$. The average segmentation results on such G-images are summarized in Fig. 13. A selected example is portrayed in Fig. 14.

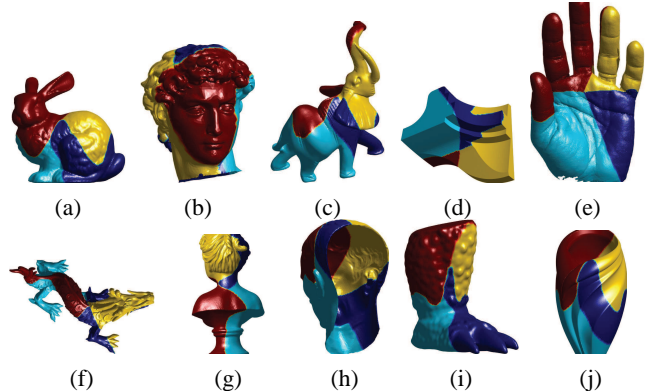


Fig. 12. Ten synthetic G-images.

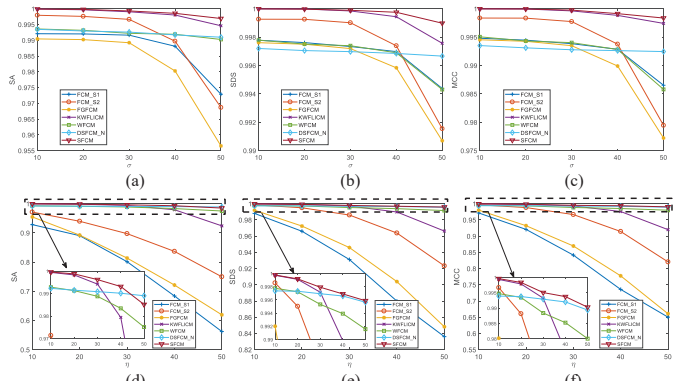


Fig. 13. Average segmentation results on ten synthetic G-images corrupted by different types of noises at different levels.

As Fig. 13 shows, when coping with complex graphs, six peers cannot suppress Gaussian noise of high levels. FCM_S1, FCM_S2 and FGFCM have no resistance to impulse noise. KWFLICM does not remove high levels of impulse noise. Compared with four above algorithms, WFCM and DSFCM_N obtain better segmentation results. In particular, DSFCM_N is robust to impulse noise of high levels since it is modelled by noise sparsity. Compared with all peers, SFCM performs the best. The visual results shown in Fig. 14 also validate the above conclusions.

D. Results on Real-world G-images

To further exhibit the segmentation ability of SFCM, we test two sets of real-world G-images with unknown noise, which

¹<http://www.graphics.stanford.edu/data/3Dscanrep/>

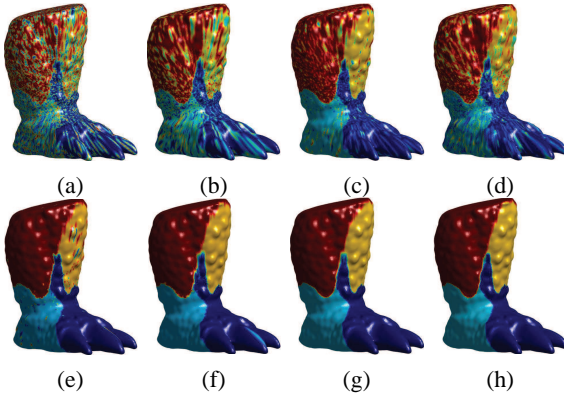


Fig. 14. Segmentation results on synthetic G-image (Fig. 12(i)) corrupted by impulse noise ($\eta = 40$ and $\alpha = 350$). From (a) to (h): observed G-image and results of FCM_S1, FCM_S2, FGFCM, KWFLICM, WFCM, DSFCM_N, and SFCM.

are borrowed from NASA Earth Observation Database². Each set corresponds to a specific scene and includes a number of G-images sampled at some point in time. Due to lack of ground truth, three standard criteria cannot be calculated directly. To deal with this issue, we collect all G-images sampled at same point in time within the time span 2000–2019. Thus, the mean G-image for some point in time is generated, which is regarded as ground truth. For real-world G-images, how to set the number of clusters depends on their actual meaning. In this experiment, we set c to 4 and 2 for segmenting the two sets of G-images, respectively. The average segmentation results for each set are given in Fig. 15. In Figs. 16 and 17, we exhibit two samples chosen from two sets.

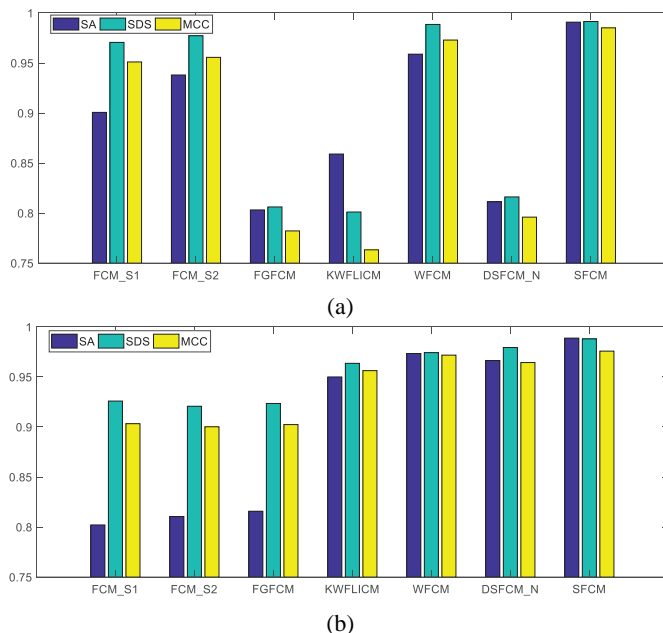


Fig. 15. Average segmentation results on two sets of real-world G-images. (a) sea ice and snow extent and (b) chlorophyll concentration.

As Fig. 15 shows, SFCM acquires better segmentation results than its six peers. When coping with the first set

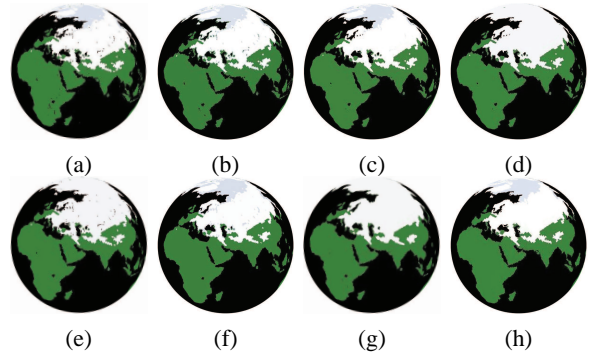


Fig. 16. Segmentation results on sea ice and snow extent in February 7–14, 2015 ($\alpha = 350$). From (a) to (h): observed G-image and results of FCM_S1, FCM_S2, FGFCM, KWFLICM, WFCM, DSFCM_N, and SFCM.

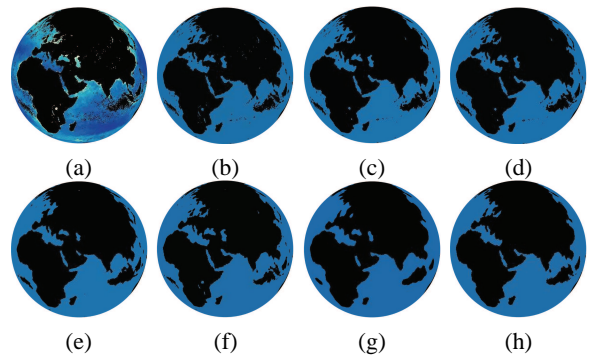


Fig. 17. Segmentation results on chlorophyll concentration in October, 2019 ($\alpha = 150$). From (a) to (h): observed G-image and results of FCM_S1, FCM_S2, FGFCM, KWFLICM, WFCM, DSFCM_N, and SFCM.

of G-images, the performance of FGFCM, KWFLICM and DSFCM_N is unsatisfactory since they yield incorrect clusters as shown in Fig. 16. Since FCM_S1, FCM_S2 and WFCM do not fully remove unknown noise, their results are not good either. As for segmenting the second set of G-images, as shown in Fig. 17, its peers give rise to several topology changes including merging and splitting, or insufficient noise removal. In conclusion, the performance of SFCM is superior to all of them.

E. Computing Overhead

To illustrate SFCM's efficiency, we provide the computing overheads of SFCM and its peers. We clarify that K is the number of G-image pixels, c is the number of prototypes, t is the iteration count, $|\mathcal{N}_i|$ denotes the size of a local window centralized at pixel i , and μ is the number of pixel levels in a G-image. Generally, $\mu \ll K$. The computational complexity of SFCM and other FCM variants is presented in Table II.

As Table II shows, FGFCM has lower computational complexity than its peers due to $\mu \ll K$. Except WFCM and SFCM, the computational complexity of other algorithms is regarded as $O(K)$. Since $O(K \log K)$ associated with a tight wavelet frame transform is close to $O(K)$, the computational complexity of WFCM and SFCM is not high. In addition, to compare the practicability between SFCM and its peers, we gather the execution time of all algorithms on tested G-images in Table III. We clarify that all experiments are performed in

²<http://neo.sci.gsfc.nasa.gov/>

TABLE II
COMPUTATIONAL COMPLEXITY OF ALL ALGORITHMS

Algorithm	Computational complexity
FCM_S1	$O(K \times \mathcal{N}_i + K \times c \times t)$
FCM_S2	$O(K \times \mathcal{N}_i + K \times c \times t)$
FGFCM	$O(K \times \mathcal{N}_i + \mu \times c \times t)$
KWFLICM	$O(K \times \mathcal{N}_i + K \times c \times t \times \mathcal{N}_i)$
WFPCM	$O(K \times \mathcal{N}_i + 3 \times K \times \log K + K \times c \times t)$
DSFCM_N	$O(K \times c \times t \times \mathcal{N}_i)$
SFCM	$O(K \times \mathcal{N}_i + 3 \times K \times \log K + K \times c \times t \times \mathcal{N}_i)$

Matlab on a laptop with Intel(R) Core(TM) i5-8250U CPU of (1.60 GHz) and 8.0 GB RAM.

TABLE III
COMPARISON OF EXECUTION TIME (IN SECONDS) OF ALL ALGORITHMS

Method	Fig. 11	Fig. 14	Fig. 16	Fig. 17
FCM_S1	4.79	7.38	8.54	4.64
FCM_S2	4.07	6.98	8.88	4.82
FGFCM	2.48	4.97	4.24	4.14
KWFLICM	67.76	102.6	298.97	54.3
WFPCM	3.12	5.56	6.64	7.1
DSFCM_N	9.52	15.25	36.65	18.9
SFCM	3.75	6.32	5.74	3.6

From Table III, we can observe that KFLICM is the most time-consuming. Its execution time is far greater than one of other peers. In contrast to it, FGFCM requires the least time since gray level histograms instead of image pixels are used in clustering. In fact, all algorithms except KWFLICM have acceptable computing overheads. SFCM requires less time than most of them. In addition, it obtains the best performance among them. Therefore, it is more practical.

F. Comparison with Non-FCM Methods

In this subsection, we compare SFCM with two non-FCM methods, i.e., PFE [45] and AMR_SC [46]. We here test two synthetic G-images and two real-world ones. Note that mixed Gaussian and impulse noise with level $\sigma = 30$ and $\eta = 20$ is added on synthetic ones. We list the comparison results on four G-images in Fig. 18 and Table IV. The computing time of SFCM, AMR_SC, and PFE is summarized in Table V. The results indicate that SFCM achieves higher effectiveness and efficiency than AMR_SC and PFE.

TABLE IV
COMPARISON OF SEGMENTATION PERFORMANCE BETWEEN SFCM AND TWO NON-FCM METHODS

Algorithm	Fig. 18 column 1			Fig. 18 column 2		
	SA	SDS	MCC	SA	SDS	MCC
AMR_SC	0.973	0.990	0.981	0.975	0.992	0.980
PFE	0.990	0.996	0.992	0.990	0.997	0.992
SFCM	0.997	0.998	0.995	0.996	0.998	0.995

Algorithm	Fig. 18 column 3			Fig. 18 column 4		
	SA	SDS	MCC	SA	SDS	MCC
AMR_SC	0.959	0.989	0.973	0.966	0.979	0.964
PFE	0.811	0.816	0.796	0.973	0.974	0.972
SFCM	0.991	0.991	0.985	0.989	0.988	0.976

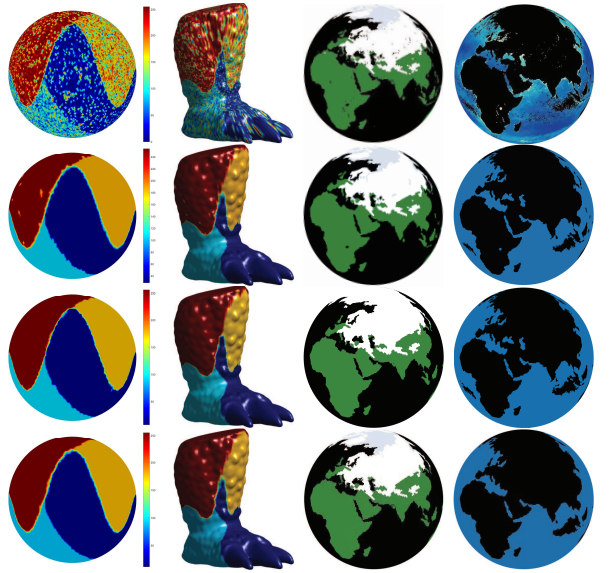


Fig. 18. Segmentation results on four G-images ($\alpha_1 = 300$, $\alpha_2 = 450$, $\alpha_3 = 350$ and $\alpha_4 = 150$). From top to bottom: observed G-images and results of AMR_SC, PFE, and SFCM.

TABLE V
COMPARISON OF EXECUTION TIME (IN SECONDS) BETWEEN SFCM AND TWO NON-FCM METHODS

Algorithm	Fig. 18 column 1	Fig. 18 column 2	Fig. 18 column 3	Fig. 18 column 4
AMR_SC	4.69	6.82	7.9	4.25
PFE	76.51	134.77	217.86	68.47
SFCM	3.59	5.07	5.74	3.6

V. CONCLUSIONS AND FUTURE WORK

In this study, we have investigated an extension of classic image segmentation, i.e., G-image segmentation. In this emerging field, we present a similarity-preserving FCM algorithm by integrating into FCM three key components, i.e., spatial information, wavelet space, and KL divergence. It optimizes the partition matrix of FCM by using KL divergence, which further enhances FCM's performance. By spatial information constraint, it becomes more robust to noise and applicable to various graphs including those with complex topologies. In addition, it can easily extract image features in a wavelet space, which benefits its performance enhancement. Experimental results well demonstrate that the proposed algorithm outperforms state-of-the-art techniques and requires less time than most of them.

Next, we report several open issues worth further pursuing. The first question is whether graph domains can be refined in more applied fields such as remote sensing [50], ecological systems [51], [52], and transportation networks [53]. Can the size of spatial information be further expanded? How can the number of clusters be selected automatically? They remain open.

REFERENCES

- [1] X. Liu, Z. Deng, and Y. Yang, "Recent progress in semantic image segmentation," *Artif. Intell. Rev.*, vol. 52, pp. 1089–1106, Aug. 2019.
- [2] H. Benninghoff and H. Garcke, "Segmentation and restoration of images on surfaces by parametric active contours with topology changes," *J. Math. Imaging Vision*, vol. 55, no. 1, pp. 105–124, May 2016.

- [3] H. Benninghoff and H. Garcke, "Segmentation of three-dimensional images with parametric active surfaces and topology changes," *J. Sci. Comput.*, vol. 72, no. 3, pp. 1333–1367, Sep. 2017.
- [4] M. Herrmann, R. Herzog, H. Kröner, S. Schmidt, and J. Vidal, "Analysis and an interior-point approach for TV image reconstruction problems on smooth surfaces," *SIAM J. Imag. Sci.*, vol. 11, no. 2, pp. 889–922, Apr. 2018.
- [5] A. Ortega, P. Frossard, J. Kovačević, J. M. F. Moura, and P. Vandergheynst, "Graph signal processing: Overview, challenges, and applications," *Proc. IEEE*, vol. 106, no. 5, pp. 808–828, May 2018.
- [6] R. R. Coifman and S. Lafon, "Diffusion maps," *Appl. Comput. Harmon. Anal.*, vol. 21, no. 1, pp. 5–30, Jul. 2006.
- [7] A. Singer, "From graph to manifold Laplacian: The convergence rate," *Appl. Comput. Harmon. Anal.*, vol. 21, no. 1, pp. 128–134, Jul. 2006.
- [8] D. K. Hammond, P. Vandergheynst, and R. Gribonval, "Wavelets on graphs via spectral graph theory," *Appl. Comput. Harmon. Anal.*, vol. 30, no. 2, pp. 129–150, Mar. 2011.
- [9] B. Dong, "Sparse representation on graphs by tight wavelet frames and applications," *Appl. Comput. Harmon. Anal.*, vol. 42, no. 3, pp. 452–479, May 2017.
- [10] C. Wang and J. Yang, "Poisson noise removal of images on graphs using tight wavelet frames," *Visual Comput.*, vol. 34, no. 10, pp. 1357–1369, Oct. 2018.
- [11] C. Wang, Z. Yan, W. Pedrycz, M. Zhou, and Z. Li, "A weighted fidelity and regularization-based method for mixed or unknown noise removal from images on graphs," *IEEE Trans. Image Process.*, vol. 29, no. 1, pp. 5229–5243, Dec. 2020.
- [12] G. B. Coleman and H. C. Andrews, "Image segmentation by clustering," *Proc. IEEE*, vol. 67, no. 5, pp. 773–785, May 1979.
- [13] M. Yambal and H. Gupta, "Image segmentation using fuzzy c means clustering: A survey," *Int. J. Adv. Res. Comput. Commun. Eng.*, vol. 2, no. 7, pp. 2927–2929, Jul. 2013.
- [14] V. Grau, A. Mewes, M. Alcaniz, R. Kikinis, and S. Warfield, "Improved watershed transform for medical image segmentation using prior information," *IEEE Trans. Med. Imag.*, vol. 23, no. 4, pp. 447–458, Apr. 2004.
- [15] D. Mahapatra, "Semi-supervised learning and graph cuts for consensus based medical image segmentation," *Pattern Recognit.*, vol. 63, pp. 700–709, Mar. 2017.
- [16] D. Pathak, P. Krähenbühl, and T. Darrell, "Constrained convolutional neural networks for weakly supervised segmentation," in *Proc. IEEE Int. Conf. Comput. Vis. (ICCV)*, Santiago, Dec. 2015, pp. 1796–1804.
- [17] M. Gong, H. Li, X. Zhang, Q. Zhao, and B. Wang, "Nonparametric statistical active contour based on inclusion degree of fuzzy sets," *IEEE Trans. Fuzzy Syst.*, vol. 24, no. 5, pp. 1176–1192, Oct. 2016.
- [18] M. Ahmed, S. Yamany, N. Mohamed, A. Farag, and T. Moriarty, "A modified fuzzy C-means algorithm for bias field estimation and segmentation of MRI data," *IEEE Trans. Med. Imag.*, vol. 21, no. 3, pp. 193–199, Aug. 2002.
- [19] S. Chen and D. Zhang, "Robust image segmentation using FCM with spatial constraints based on new kernel-induced distance measure," *IEEE Trans. Syst. Man Cybern. Part B Cybern.*, vol. 34, no. 4, pp. 1907–1916, Aug. 2004.
- [20] L. Szilagyi, Z. Benyo, S. Szilagyi, and H. Adam, "MR brain image segmentation using an enhanced fuzzy C-means algorithm," in *Proc. 25th Annu. Int. Conf. IEEE EMBS*, Sep. 2003, pp. 724–726.
- [21] W. Cai, S. Chen, and D. Zhang, "Fast and robust fuzzy c-means clustering algorithms incorporating local information for image segmentation," *Pattern Recognit.*, vol. 40, no. 3, pp. 825–838, Mar. 2007.
- [22] S. Krinidis and V. Chatzis, "A robust fuzzy local information C-means clustering algorithm," *IEEE Trans. Image Process.*, vol. 19, no. 5, pp. 1328–1337, Jan. 2010.
- [23] X. Bai, Y. Zhang, H. Liu, and Z. Chen, "Similarity measure-based possibilistic FCM with label information for brain MRI segmentation," *IEEE Trans. Cybern.*, vol. 49, no. 7, pp. 2618–2630, Jul. 2019.
- [24] M. Gong, Y. Liang, J. Shi, W. Ma, and J. Ma, "Fuzzy C-means clustering with local information and kernel metric for image segmentation," *IEEE Trans. Image Process.*, vol. 22, no. 2, pp. 573–584, Feb. 2013.
- [25] A. Elazab, C. Wang, F. Jia, J. Wu, G. Li, and Q. Hu, "Segmentation of brain tissues from magnetic resonance images using adaptively regularized kernel-based fuzzy-means clustering," *Comput. Math. Method. M.*, vol. 2015, pp. 1–12, Nov. 2015.
- [26] F. Zhao, L. Jiao, and H. Liu, "Kernel generalized fuzzy c-means clustering with spatial information for image segmentation," *Digit. Signal Process.*, vol. 23, no. 1, pp. 184–199, Jan. 2013.
- [27] F. Guo, X. Wang, and J. Shen, "Adaptive fuzzy c-means algorithm based on local noise detecting for image segmentation," *IET Image Process.*, vol. 10, no. 4, pp. 272–279, Apr. 2016.
- [28] Z. Zhao, L. Cheng, and G. Cheng, "Neighbourhood weighted fuzzy c-means clustering algorithm for image segmentation," *IET Image Process.*, vol. 8, no. 3, pp. 150–161, Mar. 2014.
- [29] R. R. Gharieb and G. Gendy, "Fuzzy C-means with a local membership KL distance for medical image segmentation," in *Proc. IEEE Int. Biomed. Eng. Conf. (CIBEC)*, Cairo, Dec. 2014. doi: 10.1109/CIBEC.2014.7020912
- [30] R. R. Gharieb, G. Gendy, A. Abdelfattah, and H. Selim, "Adaptive local data and membership based KL divergence incorporating C-means algorithm for fuzzy image segmentation," *Appl. Soft Comput.*, vol. 59, pp. 143–152, Oct. 2017.
- [31] C. Wang, W. Pedrycz, Z. Li, and M. Zhou, "Kullback-Leibler divergence-based Fuzzy C-Means clustering incorporating morphological reconstruction and wavelet frames for image segmentation," arXiv preprint arXiv:2002.09479, 2020.
- [32] J. Gu, L. Jiao, S. Yang, and F. Liu, "Fuzzy double c-means clustering based on sparse self-representation," *IEEE Trans. Fuzzy Syst.*, vol. 26, no. 2, pp. 612–626, Apr. 2018.
- [33] Y. Zhang, X. Bai, R. Fan, and Z. Wang, "Deviation-sparse fuzzy c-means with neighbor information constraint," *IEEE Trans. Fuzzy Syst.*, vol. 27, no. 1, pp. 185–199, Jan. 2019.
- [34] C. Wang, W. Pedrycz, M. Zhou, and Z. Li, "Sparse regularization-based Fuzzy C-Means clustering incorporating morphological grayscale reconstruction and wavelet frames," *IEEE Trans. Fuzzy Syst.*, to be published, doi: 10.1109/TFUZZ.2020.2985930.
- [35] T. Lei, X. Jia, Y. Zhang, L. He, H. Meng, and K. N. Asoke, "Significantly fast and robust fuzzy c-means clustering algorithm based on morphological reconstruction and membership filtering," *IEEE Trans. Fuzzy Syst.*, vol. 26, no. 5, pp. 3027–3041, Oct. 2018.
- [36] C. Wang, W. Pedrycz, Z. Li, M. Zhou, and J. Zhao, "Residual-sparse Fuzzy C-Means clustering incorporating morphological reconstruction and wavelet frames," arXiv preprint arXiv:2002.08418, 2020.
- [37] T. Lei, P. Liu, X. Jia, X. Zhang, H. Meng, and A. K. Nandi, "Automatic fuzzy clustering framework for image segmentation," *IEEE Trans. Fuzzy Syst.*, to be published, doi: 10.1109/TFUZZ.2019.2930030.
- [38] C. Wang, W. Pedrycz, J. Yang, M. Zhou, and Z. Li, "Wavelet frame-based fuzzy C-means clustering for segmenting images on graphs," *IEEE Trans. Cybern.*, vol. 50, no. 9, pp. 3938–3949, Sep. 2020.
- [39] A. Ron and Z. Shen, "Affine systems in $L_2(\mathbb{R}^d)$: The analysis of the analysis operator," *J. Funct. Anal.*, vol. 148, no. 2, pp. 408–447, Aug. 1997.
- [40] J. F. Cai, B. Dong, S. Osher, and Z. Shen, "Image restoration: total variation, wavelet frames, and beyond," *J. Amer. Math. Soc.*, vol. 25, no. 4, pp. 1033–1089, May 2012.
- [41] J. Yang and C. Wang, "A wavelet frame approach for removal of mixed Gaussian and impulse noise on surfaces," *Inverse Probl. Imaging*, vol. 11, no. 5, pp. 783–798, Oct. 2017.
- [42] J. C. Bezdek, R. Ehrlich, and W. Full, "FCM: The fuzzy C-means clustering algorithm," *Comput. Geosci.*, vol. 10, no. 2-3, pp. 191–203, 1984.
- [43] J. C. Mason and D. C. Handscomb, *Chebyshev Polynomials*. London: Chapman and Hall, 2003.
- [44] J. Yang, G. Zhu, D. Tong, L. Lu, and Z. Shen, "B-spline tight frame based force matching method," *J. Comput. Phys.*, vol. 362, no. 1, pp. 208–219, Jun. 2018.
- [45] C. Fang, Z. Liao, and Y. Yu, "Piecewise flat embedding for image segmentation," *IEEE Trans. Pattern Anal. Mach. Intell.*, vol. 41, no. 6, pp. 1470–1485, Jun. 2019.
- [46] T. Lei, X. Jia, T. Liu, S. Liu, H. Meng, and A. K. Nandi, "Adaptive morphological reconstruction for seeded image segmentation," *IEEE Trans. Image Process.*, vol. 28, no. 11, pp. 5510–5523, Nov. 2019.
- [47] D. N. H. Thanh, D. Sergey, V. B. S. Prasath, and N. H. Hai, "Blood vessels segmentation method for retinal fundus images based on adaptive principal curvature and image derivative operators," *Int. Arch. Photogramm. Remote Sens. Spatial Inf. Sci.*, vol. XLII-2/W12, pp. 211–218, May 2019. doi: 10.5194/isprs-archives-XLII-2-W12-211-2019
- [48] D. N. H. Thanh, U. Erkan, V. B. S. Prasath, V. Kumar, and N. N. Hien, "A skin lesion segmentation method for dermoscopic images based on adaptive thresholding with normalization of color models," in *Proc. IEEE 6th Int. Conf. Electr. Electron. Eng.*, Apr. 2019, pp. 116–120.
- [49] C. Wang, W. Pedrycz, Z. Li, and M. Zhou, "Residual-driven Fuzzy C-Means clustering for image segmentation," *IEEE/CAA J. Autom. Sinica*, to be published, doi: 10.1109/JAS.2020.1003420.

- [50] T. Xu, L. Jiao, and W. J. Emery, "SAR image content retrieval based on fuzzy similarity and relevance feedback," *IEEE J. Sel. Topics Appl. Earth Observ. Remote Sens.*, vol. 10, no. 5, pp. 1824–1842, May 2017.
- [51] C. Wang, J. Chen, Z. Li, E. Nasr, and A. M. El-Tamimi, "An indicator system for evaluating the development of land-sea coordination systems: A case study of Lianyungang port," *Ecol. Indic.*, vol. 98, pp. 112–120, Mar. 2019.
- [52] A. K. Bhandari, A. Ghosh, and I. V. Kumar, "A local contrast fusion based 3D Otsu algorithm for multilevel image segmentation," *IEEE/CAA J. Autom. Sinica*, vol. 7, no. 1, pp. 200–213, January 2020.
- [53] Y. Lv, Y. Chen, X. Zhang, Y. Duan, and N. Li, "Social media based transportation research: the state of the work and the networking," *IEEE/CAA J. Autom. Sinica*, vol. 4, no. 1, pp. 19–26, Jan. 2017.



Cong Wang received the B.S. degree in automation and the M.S. degree in mathematics from Hohai University, Nanjing, China, in 2014 and 2017, respectively. He is currently pursuing the Ph.D. degree in mechatronic engineering, Xidian University, Xi'an, China.

He was a Visiting Ph.D. Student in the Department of Electrical and Computer Engineering, University of Alberta, Edmonton, AB, Canada. He was also a Research Assistant at the School of Computer Science and Engineering, Nanyang Technological University, Singapore. He is currently a Visiting Ph.D. Student in the Department of Electrical and Computer Engineering, National University of Singapore, Singapore. His current research interests include wavelet analysis and its applications, granular computing, as well as image processing.



ZhiWu Li (Fellow, IEEE) received the B.S. degree in mechanical engineering, the M.S. degree in automatic control, and the Ph.D. degree in manufacturing engineering from Xidian University, Xi'an, China, in 1989, 1992, and 1995, respectively.

He joined Xidian University in 1992. He is also currently with the Institute of Systems Engineering, Macau University of Science and Technology, Macau, China. He was a Visiting Professor with the University of Toronto, Toronto, ON, Canada, the Technion-Israel Institute of Technology, Haifa, Israel, the Martin-Luther University of Halle-Wittenberg, Halle, Germany, Conservatoire National des Arts et Métiers, Paris, France, and Meliksah Universitesi, Kayseri, Turkey. His current research interests include Petri net theory and application, supervisory control of discrete-event systems, workflow modeling and analysis, system reconfiguration, game theory, and data and process mining.

Dr. Li was a recipient of an Alexander von Humboldt Research Grant, Alexander von Humboldt Foundation, Germany. He is listed in Marquis Who's Who in the World, 27th Edition, 2010. He serves as a Frequent Reviewer of 90+ international journals, including Automatica and a number of the IEEE TRANSACTIONS as well as many international conferences. He is the Founding Chair of Xi'an Chapter of IEEE Systems, Man, and Cybernetics Society. He is a member of Discrete-Event Systems Technical Committee of the IEEE Systems, Man, and Cybernetics Society and IFAC Technical Committee on Discrete-Event and Hybrid Systems, from 2011 to 2014.



Witold Pedrycz (Fellow, IEEE) received the M.Sc. degree in computer science and technology, the Ph.D. degree in computer engineering, and the D.Sci. degree in systems science from the Silesian University of Technology, Gliwice, Poland, in 1977, 1980, and 1984, respectively.

He is a Professor and the Canada Research Chair in Computational Intelligence with the Department of Electrical and Computer Engineering, University of Alberta, Edmonton, AB, Canada. He is also with the Systems Research Institute of the Polish Academy of Sciences, Warsaw, Poland. He is a foreign member of the Polish Academy of Sciences. He has authored 15 research monographs covering various aspects of computational intelligence, data mining, and software engineering. His current research interests include computational intelligence, fuzzy modeling, and granular computing, knowledge discovery and data mining, fuzzy control, pattern recognition, knowledge-based neural networks, relational computing, and software engineering. He has published numerous papers in the above areas.

Dr. Pedrycz was a recipient of the IEEE Canada Computer Engineering Medal, the Cajastur Prize for Soft Computing from the European Centre for Soft Computing, the Killam Prize, and the Fuzzy Pioneer Award from the IEEE Computational Intelligence Society. He is intensively involved in editorial activities. He is an Editor-in-Chief of Information Sciences, an Editor-in-Chief of WIREs Data Mining and Knowledge Discovery (Wiley) and the International Journal of Granular Computing (Springer). He currently serves as a member of a number of editorial boards of other international journals. He is a fellow of the Royal Society of Canada.



MengChu Zhou (Fellow, IEEE) received his B.S. degree in Control Engineering from Nanjing University of Science and Technology, Nanjing, China, in 1983, M.S. degree in Automatic Control from Beijing Institute of Technology, Beijing, China, in 1986, and Ph. D. degree in Computer and Systems Engineering from Rensselaer Polytechnic Institute, Troy, NY, USA, in 1990, respectively.

He joined New Jersey Institute of Technology (NJIT), Newark, NJ, in 1990, and is now a Distinguished Professor of Electrical and Computer Engineering. His research interests are in Petri nets, intelligent automation, Internet of Things, big data, web services, and intelligent transportation.

He has over 900 publications including 12 books, 600+ journal papers (450+ in IEEE TRANSACTIONS), 26 patents and 29 book-chapters. He is the founding Editor of IEEE Press Book Series on Systems Science and Engineering, Editor-in-Chief of IEEE/CAA Journal of Automatica Sinica, and Associate Editor of IEEE Internet of Things Journal, IEEE Transactions on Intelligent Transportation Systems, and IEEE Transactions on Systems, Man, and Cybernetics: Systems. He is a recipient of Humboldt Research Award for US Senior Scientists from Alexander von Humboldt Foundation, Franklin V. Taylor Memorial Award and the Norbert Wiener Award from IEEE Systems, Man and Cybernetics Society, and Excellence in Research Prize and Medal from NJIT. He is a life member of Chinese Association for Science and Technology-USA and served as its President in 1999. He is a Fellow of International Federation of Automatic Control (IFAC), American Association for the Advancement of Science (AAAS) and Chinese Association of Automation (CAA).



Shuzhi Sam Ge (Fellow, IEEE) received the B.Sc. degree from the Beijing University of Aeronautics and Astronautics, Beijing, China, in 1986, and the Ph.D. degree from Imperial College London, London, U.K., in 1993.

He is the Director of the Social Robotics Laboratory of Interactive Digital Media Institute, Singapore, and the Centre for Robotics, Chengdu, China, and a Professor with the Department of Electrical and Computer Engineering, National University of Singapore, Singapore, on leave from the School of Computer Science and Engineering, University of Electronic Science and Technology of China, Chengdu. He is an Honorary Professor with the Institute of Future, Qingdao University, Qingdao, China. He has coauthored 4 books and over 300 international journals and conference papers. His current research interests include social robotics, adaptive control, intelligent systems, and artificial intelligence.

Prof. Ge is an Editor-in-Chief of the *International Journal of Social Robotics* (Springer). He has served/been serving as an Associate Editor for a number of flagship journals, including the IEEE TRANSACTIONS ON AUTOMATIC CONTROL, the IEEE TRANSACTIONS ON CONTROL SYSTEMS TECHNOLOGY, the IEEE TRANSACTIONS ON NEURAL NETWORKS, and *Automatica*. He serves as a Book Editor for the Taylor and Francis Automation and Control Engineering Series. He served as the Vice President for Technical Activities from 2009 to 2010, the Vice President of Membership Activities, from 2011 to 2012, and a member of the Board of Governors from 2007 to 2009 at the IEEE Control Systems Society. He is a Fellow of the International Federation of Automatic Control, the Institution of Engineering and Technology, and the Society of Automotive Engineering.